PdCu single atom alloys supported on alumina for the selective hydrogenation of furfural

Mohammed J. Islam[a], Marta Granollers Mesa[a*], Amin Osatiashtiani[a], Jinesh C. Manayil[a], Mark A. Isaacs[b,c], Martin J. Taylor[d], Sotirios Tsatsos[e] and Georgios Kyriakou[a,e*]

[a] Energy & Bioproducts Research Institute (EBRI), Aston University, Aston Triangle, Birmingham, B4 7ET, United Kingdom

[b] Department of Chemistry, University College London, London, WC1H 0AJ, United Kingdom

[c] HarwellXPS, Research Complex at Harwell, Rutherford Appleton Labs, Didcot, OX11 0FA, United Kingdom

[d] Energy and Environment Institute, University of Hull, Cottingham Road, Hull, HU6 7RX, United Kingdom

[e] Department of Chemical Engineering, University of Patras, Caratheodory 1, Patras GR 265 04, Greece

[*]Corresponding authors, E-mail address: m.granollers-mesa@aston.ac.uk (M. Granollers Mesa), kyriakg@upatras.gr (G. Kyriakou)

Abstract

Single-atom catalysts serve as a skilful control of precious metals on heterogenous catalysts where all active sites are accessible for catalytic reactions. Here we report the adoption of PdCu single-atom alloys supported on alumina for the selective hydrogenation of furfural. This is a special class of an atom efficient, single-site catalyst where trace concentrations of Pd atoms (0.0067 wt%) displace surface Cu sites on the host nanoparticle. Confirmed by EXAFS, the Pd atoms are entirely coordinated to Cu, with Pd-Cu bond lengths identical to that of a Cu-Cu bond. Selectively surface oxidised catalysts also confirm surface Pd atoms by EXAFS. These catalysts improve the conversion of furfural to furfuryl alcohol compared to monometallic catalysts, as they have the advantages of Cu (high selectivity but poor activity) and Pd catalysts (superior activity but unselective) without the drawbacks, making them the optimal catalysts for green/atom efficient catalysis.

Keywords

Palladium; Copper; Furfural; Hydrogenation; Single-Atom Catalysts

1 Introduction

The growth in population together with the increased need for energy, chemicals and pharmaceuticals are the main drives towards a bio-based economy [1]. The shift away from non-renewable petroleum and natural gas resources has a significant impact on the chemical industry's reliant on them [2]. As a result, the development of novel catalytic processes is

crucial to transform raw bio-based resources into sustainable fuels and chemicals. One of the biomass-derived platform chemicals identified by the U.S. Department of Energy is furfural [3], a molecule of crucial interest from the pyrolysis of hemicellulose components in lignocellulosic biomass waste [4-7], where ~62% of its global consumption is selectively hydrogenated to furfuryl alcohol [8]. Furfuryl alcohol is a transient molecule used to synthesise ascorbic acid and anti-corrosive coatings but primarily for furan based resins [9, 10]. Over the past 90 years, current industrial processes for the selective hydrogenation to furfuryl alcohol have used copper chromite catalysts [9, 11-13] operating energy-intensive conditions of 200 °C, and hydrogen pressures up to 30 bar [2]. However, such chromite-based catalysts over time deteriorate and release chromic oxide, a highly toxic compound that causes severe environmental problems and contamination of the resulting products. Therefore, there is motivation to develop an environmentally friendly, energy-efficient catalytic materials which adapt to milder reaction conditions.

Many alternatives to the currently utilised chromite-based catalysts have been investigated in the literature for the hydrogenation of furfural including Ir, Pt, Pd, Ru, Ni, Cu, Co and Mo [2, 6, 14-30]. In most cases, only the surface atoms of the nanoparticle are the active sites, while those in the nanoparticle bulk are spectators. For example, in a 5 nm particle only about 22% of the atoms are available for catalysis, which leads to an inefficient use of precious metals. However, when more abundant elements (e.g. Cu) are used, they often require harsher conditions such as temperature/pressure or augmenting their catalytic activity with precious metals [6]. A method of improving atom efficiency is to increase the dispersity of catalysts up to the atomic limit. This is where single-atom catalysis exists, blurring the lines between traditional heterogeneous and homogeneous catalysis [31]. Several studies have been reported whether a single atom attached to the support would work as an efficient catalyst for various catalytic processes [32-34] such as the water-gas shift reaction. Flytzani-Stephanopolous et al. [35] found that single atoms of Au, present as surface Au-O_x species could be used for the low-temperature water-gas shift reaction. During this investigation, the authors found no evidence of Au nanoparticles taking part as active species. Various other studies have investigated single-atom catalysts (SAC) both theoretically and experimentally looking for new preparation methods and catalytic/redox processes [36-41]. Additionally, various Pd ensemble sizes have also been studied previously ranging from nanoparticles to clusters to single atoms which were used for the transformation of aldehydes [42, 43]. Typically, introducing high Pd content on the host metal surface leads to a distribution of Pd ensembles, in which single Pd atoms coexist

with dimers, trimers, and even higher Pd clusters [44]. Advantages of single atoms include incredible activity [45] with chemoselectivity towards the desired products (for example hydrogenation of nitroarenes) due to their isolated active sites. As one can expect, there is better active site control compared to a nanoparticle where there are different surface planes each exhibiting different electronic and chemical environments and thus leading to different reactivities. A subclass of SACs supported on typically a base metal such as copper were reported initially by Kyriakou et al. [44]. Here, Pd atoms were deposited on a Cu (111) surface under Ultra High Vacuum (UHV) conditions, where they observed stable isolated Pd species via Low Temperature-Scanning Tunnelling Microscopy (LT-STM), naming the structure a single-atom alloy (SAA). Various DFT studies also supported their findings that the isolated Pd atoms present can act as entry and exit sites for hydrogen dissociation and recombination with the reported activation energy falling from 0.4 eV (Cu 111) to ~0.02 eV with the SAA [39, 44, 46, 47]. These fundamental experiments in UHV led to the development of practical SAA catalysts used in various catalytic reactions [38, 41, 48, 49].

In an earlier investigation we reported the use of a range of supported PtCu bimetallic nanoparticles including Ultra Dilute Alloy (UDA) for the liquid-phase selective hydrogenation of furfural. In the case of UDAs alloying was achieved by the galvanic replacement of Cu atoms by Pt atoms on host Cu nanoparticles. In the case of UDA catalysts, despite the very low content of Pt (atomic ratio between Pt:Cu ~ 1:20), displayed minimal clustering of Pt on the surface of the nanoparticle and were found to exhibits exceptionally high initial rates of hydrogenation rivalling the catalytic turnover of the monometallic Pt nanoparticles. The present work investigates the development of atom efficient PdCu SAA catalysts for the selective hydrogenation of furfural in the liquid phase. In this case the Pd content in the nanoparticle is minimised to the extent that Pd exists as single atomic entities on the Cu host nanoparticle. We have used copper as the host nanoparticle since it is well known that these catalysts are very selective due to the η^1(O)-aldehyde binding mode [50, 51] of furfural to the surface promoting C=O hydrogenation. As the result of hydrogen dissociation being an activated process on Cu surfaces, the isolated Pd atoms enhance hydrogen dissociation spillover onto the copper surface, increasing the activity of the catalyst. Experiments will also be conducted to optimise the catalytic behaviour by adjusting synthetic parameters. Due to the lack of experimental studies on whether the isolated surface Pd atoms can sink into the nanoparticle, XAS experiments will be used to give insight into this. While various combinations of non-toxic catalysts have previously been investigated, including PdCu [52],

the implementation of single palladium atoms at trace amounts on copper host nanoparticles provides advancements in sustainability, efficiency and reactivity for the hydrogenation of furfural.

2 Experimental

2.1 Catalyst synthesis

Colloidal Cu nanoparticles were synthesised using a method reported earlier by Kanzaki et al. [53]. DL-1-Amino-2-propanol (AmIP, 2.93 mL, 99.9%, Acros Organics) was added to 7.73 mL of ethylene glycol. Cu (II) acetate (0.6811 g, 98%, Sigma-Aldrich) was then added to the mixture, forming a dark-blue solution after ultra-sonication. Once the Cu (II) acetate was dissolved, hydrazine monohydrate (1.83 mL, 98%, Alfa Aesar) was added under vigorous stirring (1100 RPM) and was left to react for ~24 h at room-temperature. The Cu nanoparticle mixture was then precipitated out by adding it to 25 mL of N, N-dimethylacetamide (DMA, 99%, Acros Organics) under gentle stirring. The copper nanoparticles were collected via centrifugation and then purified using 25 mL of DMA, toluene (HPLC grade, Fisher Chemical) and hexane (HPLC grade, Fisher Chemical). The resulting nanoparticles were then suspended in 10 mL of ethanol (HPLC grade, Fisher Chemical) by sonication. Al_2O_3 (9.9 g, 99.5%, 32-40 $m^2\ g^{-1}$, NanoArc, Alfa Aesar) was then impregnated with the nanoparticle solution (6.6 mL) after the support was mixed with 60 mL of ethanol. The ethanol was then evaporated at room temperature. Finally, the resulting solid was calcined at 300 °C (5 °C/min) for 4 h in a muffle furnace to remove residual synthetic components and reduced at 245 °C (5 °C/min) for 3 h under flowing H_2 (40 mL/min).

Supported Pd nanoparticles on Al_2O_3 were synthesised using a method previously reported for Pt nanoparticles [6, 54]. Briefly, 10 mL of ethylene glycol and 50 µL of aqueous NaOH (1 M) was refluxed at 120 °C. To the hot ethylene glycol, a solution of Na_2PdCl_4 (10.6 mM, 99.99%, Sigma Aldrich) and polyvinylpyrrolidone (PVP) (91 mM, 40,000 MW, Alfa Aesar) in a 9:1 per volume of ethylene glycol:water was added slowly over the course of an hour. The mixture turned black and was stirred for an additional 20 mins and cooled to room temperature. The nanoparticles were then isolated and cleaned with multiple acetone washes and centrifugation, the resulting solid residue was dispersed in EtOH. The support (Al_2O_3,

NanoArc™) was impregnated with the nanoparticle suspension and dried overnight. Finally, the Pd rich catalyst, Pd_{100}/Al_2O_3, was calcined at 300 °C (5 °C/min) for 4 h in a muffle furnace.

The PdCu single atom alloy catalysts were synthesised using galvanic replacement (GR) [6, 38]. The Cu/Al_2O_3 catalyst was initially reduced *in situ* at 245 °C under flowing H_2 for 3 h in a round-bottom flask. The vessel was then cooled to room temperature under flowing H_2. The flask was then purged with N_2 and heated to 100 °C, followed by the addition of deionised water (18 mL) and stirring at 700 RPM. The desired amount of Pd (II) nitrate hydrate (99.9%, Alfa Aesar) was dissolved in an aqueous 2 mM HCl solution and 2 mL of this solution was added to the reduced Cu/Al_2O_3 mixture and allowed to react/reflux for 20 min under an N_2 atmosphere. Specifically, 0.28 mg, 0.53 mg and 1.38 mg of Pd nitrate (II) hydrate was added to the reduced host Cu/Al_2O_3 (1g) mixture to make the Pd_1Cu_{234}, Pd_1Cu_{216} and Pd_1Cu_{53} catalysts, respectively. The subsequent mixture was cooled to room temperature where the catalysts were washed with deionised water (300 mL) and dried under *vacuo* followed by further drying in an oven at 60 ºC overnight.

The monometallic Cu/Al_2O_3 and Pd/Al_2O_3 catalysts were denoted Cu_{100} and Pd_{100}, respectively. While the bimetallic catalysts were denoted Pd_1Cu_n where n indicates the proportion of Cu atoms per Pd atom present. The calcination temperature was chosen based on previous works with carbonous capping agents [2]. An initial lower reduction temperature (245 °C) for the Cu catalyst was chosen for an extended duration of 3 h as it was reported to be suitable for the subsequent Pd galvanic replacement [41]. It should be noted before catalytic tests all the catalysts were in-situ reduced at 300 °C, to ensure the metallic phases are present.

2.2 Material characterisation

Samples were analysed by scanning transmission electron microscopy (STEM) using a Cs aberration-corrected JEOL 2100F microscope at 200 kV. Images were collected using a Gatan Ultrascan 4000 digital camera operated by Digital Micrograph software. Samples were dispersed in methanol (HPLC grade, Fisher Chemical) and deposited on 300-mesh carbon-supported copper grids and dried at 60 °C. ImageJ 1.52a software was used for image analysis. TEM images were also recorded on a JEOL, JEM-2100 high-resolution system (HR-TEM). Metal contents were determined by Inductively Coupled Plasma Optical Emission Spectroscopy (ICP-OES) using a Thermo Scientific iCAP 7400 Duo in both axial (increases sensitivity at low concentrations) and radial mode for Pd and Cu content, respectively. To prepare the samples for ICP-OES analysis, 3 mL HCl (37%, VWR Chemicals), 1 mL HNO_3

(68%, VWR Chemicals) and 5 mL H_2SO_4 (>95%, Fisher Scientific) were added to ~10 mg of the catalyst. The mixture was then heated to 250 °C for 1 h to ensure the complete dissolution of Al_2O_3. After cooling to room temperature, the digestate was topped to 10 mL with distilled water to account for any evaporation losses. Surface area of the support was analysed via N_2 physisorption using a Quantachrome Nova 4000 instrument, after sample outgassing at 120 °C for 2 h before analysis at –196 °C. Surface areas were calculated using the Brunauer–Emmett–Teller (BET) method over the range P/P_0 = 0.03–0.18, where a linear relationship was maintained. H_2-temperature programmed reduction (TPR) data was collected on a Quantachrome ChemBET Pulsar equipped with a TCD detector (150 mA). The catalyst (~100 mg) was loaded into a quartz wool plugged u-shaped glass tube and degassed/dried under N_2 flow at 100 °C for 30 min. TPR analysis was subsequently conducted under 5%H_2/95% N_2 (40 mL min^{-1}) at a heating rate of 6 °C min^{-1} to 300 °C. Thermal gravimetric analysis (TGA) was conducted on a Mettler Toledo TGA/DSC1 Star System under a N_2 purge gas (60 mL min^{-1}) interfaced to a ThermoStar TM GSD 301 T3 mass spectrometer. The colloidally capped Cu/Al_2O_3 catalyst (20 mg) was loaded into alumina crucible and heated from 40 – 800 °C at 10 °C min^{-1} and the dead time between the TGA and MS was assumed to be negligible. X-ray photoelectron spectroscopy (XPS) and X-ray excited Auger spectroscopy (XAES) spectra were acquired on a Kratos AXIS Supra spectrometer equipped with a charge neutraliser and monochromated Al Kα excitation source (1486.7 eV) with energies referenced to adventitious carbon at 284.8 eV using CasaXPS version 2.3.19PR1.0 and a U 2 Tougaard background. The modified auger parameter α' was defined as the sum of the photoelectron binding energy and the auger electron kinetic energy [55]. The extra-atomic relaxation energy was defined as half the change in the modified auger parameter compared to bulk Cu [56].

Powder X-ray diffraction data were collected using a Bruker D8 Advance Bragg–Brentano diffractometer equipped with a Lynxeye PSD detector and with Cu $K\alpha_{1,2}$ radiation (40 kV and 40 mA, 0.2 mm Ni K_β absorber, 2.5° Soller Slits, 10−80° 2θ range, a virtual step scan of 0.02° 2θ, virtual time per step of 8 s. The arithmetic mean domain size of the nanoparticles was determined via the Whole Powder Pattern Modelling (WPPM) method [57, 58], utilising the PM2K software [59] and described in our previous work [22]. The complex background was partially removed using OriginPro and then synthesised using a Chebyshev polynomial. The crystalline domains were assumed to be spherical and distributed according to a log-normal size distribution. The volume-weighted crystallite size was estimated with the integral breadth method (see supplementary information). X-ray absorption spectra were collected at B18 XAS

beamline at Diamond Light Source, United Kingdom. A double-crystal Si(311) monochromator was used to scan X-ray energy from –200 to 800 eV relative to the Pd K-edge (24350 eV). Following *ex situ* reduction, samples were loaded into 3 mm capillaries and the XAS measurement was conducted in fluorescence mode (multi-element Ge detector at 45° to the sample) with five scans. Pseudo-*in situ* XAS was conducted using a gas-tight cell with aluminised Kapton windows; the catalysts were pelletised and reduced in 5%H_2/95%He at 300 °C, and transferred into the cell without exposing the catalysts to atmospheric oxygen in an N_2 filled glove box. Spectra of 35 scans were collected in fluorescence mode. XAS data were analysed with Athena and Artemis, FEFF6 code [60], the accompanying reference spectra were calibrated to 24350 eV via the 2nd derivation method, aligned and merged before analysis. FEFF scattering paths were calculated using Cu and CuO CIF files, and with the absorber replaced with Pd. Samples denoted re-oxidised and reduced were analysed *ex situ* using a capillary and a gas-tight pellet cell, respectively.

2.3 Catalytic testing

In situ reduction and all catalytic reactions were carried out in a Hel DigiCAT high-pressure parallel reactor system, housing a bank of two 50 mL stainless steel reactor vessels. The reaction conditions used in this work were similar to those used in earlier studies in the literature [2, 6, 22] and provide a benchmark to compare the catalytic activity and make correlations with the nanoparticle structure, catalyst composition and recyclability. The vessels were loaded with ~30 mg of the catalyst, heated under flowing H_2 to 300 °C at 5 °C min^{-1} and held for 0.5 h before cooling to room temperature under flowing H_2. The autoclaves were subsequently sealed and purged with H_2 to prevent the oxidation of the catalyst. While H_2 was flowing, 10 mL of the reaction mixture comprising of methanol (Fisher Scientific, 99.99%), furfural (0.02 M, Sigma Aldrich, 99%) and butanol as the internal standard (0.02 M, Alfa Aesar, 99%), were injected into each reactor. The weight percent of the catalyst, reactant, internal standard and solvent at the starting point were 0.38%, 0.24%, 0.18% and 99.20%, respectively. The mixture was degassed for 10 min before pressurising under H_2 (1.5 bar, BOC, 99.995%), followed by heating to 50 °C and stirring at 600 rpm. The reactions were all carried out for 7 h at 50 °C before being cooled and depressurised to atmospheric pressure. The external mass transfer was assessed by changing the stirring speed from 600 to 900 rpm and no appreciable differences were detected within this range. The internal mass transfer was considered negligible as the catalyst is in non-porous and in powder form (40 nm), which means that all the active sites are accessible in the external surface of the support. Aliquots of

the reaction mixture (0.2 mL) were periodically taken and analysed with 1:10 dilution in methanol on a Shimadzu GC-2010 Plus equipped with a flame ionisation detector (FID) and a Zebron ZB-WAX capillary column (5%-phenyl-95%-dimethylpolysiloxane, 30 m × 0.53 mm × 1.50 μm). The concentration of the products was determined through the normalisation of the individual peak areas with the internal standard, as well as the use of 5-point calibration standards of the pure compounds. Reaction mixtures were further analysed by GCMS on a Shimadzu GCMS-QP2010 SE.

3 Results and discussions

3.1 Characterisation of alumina supported catalysts

3.1.1 Elemental, Surface Area, Particle Size and TGA-MS Analysis

Bulk elemental analysis of the catalytic materials (**Error! Reference source not found.**) shows that the Cu and Pd monometallic catalysts with an approximate loading of 1 wt% were successfully synthesised.

Table 1 Bulk elemental analysis, Pd/Cu crystallite and particle size analysis for the catalysts.

Catalyst	Pd loading[a] (wt%)	Cu loading[a] (wt%)	Pd:Cu atomic ratio	Pd crystallite/particle size (nm)	Cu crystallite/particle size (nm)
Cu_{100}	-	0.9403 ± 0.0267	-	-	2.7 ± 0.7[d]
Pd_1Cu_{234}	0.0064 ± 0.0006	0.8947 ± 0.0253	1:234	-	22.8 ± 2.3[b] 2.3 ± 2.7[c] 2.6 ± 0.7[d]
Pd_1Cu_{216}	0.0067 ± 0.0006	0.8599 ± 0.0262	1:216	-	23.7 ± 2.4[b] 2.0 ± 2.4[c] 2.0 ± 0.6[d]
Pd_1Cu_{53}	0.0296 ± 0.0022	0.9296 ± 0.0232	1:53	-	19.7 ± 2.0[b] 15.2 ± 8.4[c] 7.0 ± 4.4[d]
Pd_{100}	0.8882 ± 0.0529	-	-	14.0 ± 1.4[b] 14.0 ± 6.4[c] 5.1 ± 2.7[d]	-

[a] Determined by ICP-OES, [b] Integral breath method via XRD, [c] WPPM via XRD, [d] STEM/TEM

Bimetallic $PdCu/Al_2O_3$ catalysts show trace quantities of Pd being incorporated into the monometallic host Cu/Al_2O_3 catalyst giving Pd:Cu atomic ratios of 1:234, 1:216 and 1:53. In Fig. S1 a type II isotherm was observed for the bare support with a surface area of 38.2 m^2g^{-1} showing that the support material is non-porous. The TGA-MS of the 1-amino-2-propanol (C_3H_9NO) capped Cu nanoparticles showed it mainly decomposed into NO, and CO_2 under N_2 flow (Fig. S2).

3.1.2 H_2 Temperature Programmed Reduction (H_2-TPR)

The H_2-TPR profile shown in Fig. 1 (a) of the Pd_{100} catalyst shows that Pd can reduce at room temperature under flowing H_2, which has also been reported earlier [14]. The Pd_{100} catalyst shows a sharp negative peak at 94 °C. The physical meaning of the negative peak indicates H_2 is being released from the sample while a positive peak is H_2 consumption detected via changes in the thermal conductivity of the gas [14, 61-63]. However, this negative decomposition peak is not observed for the SAA catalysts which suggests that such features are below the detection limit (trace Pd loading) and possibly due to the hydride species needing extended Pd surfaces to form [64]. TPR profiles also show that the T_{max} for reduction (positive peaks) of the catalysts is observed to decrease with increasing Pd loading. It is also worth noting that for SAA catalysts the hydrogen consumption starts at a relatively lower temperature for the Pd_1Cu_{53} (80 °C) compared to the Pd_1Cu_{216} catalyst (100 °C). Similarly, the beginning of H_2 consumption in the case of Pd_1Cu_{234} (120 °C) is lower compared to Pd_1Cu_{216} (100 °C). This shows a strong dependency between the Pd content of the surface and temperature at which the SAA starts to consume hydrogen. The higher the concentration of single Pd entities on the Cu surface allows for easier hydrogen adsorption and spillover onto the Cu surface [44, 47].

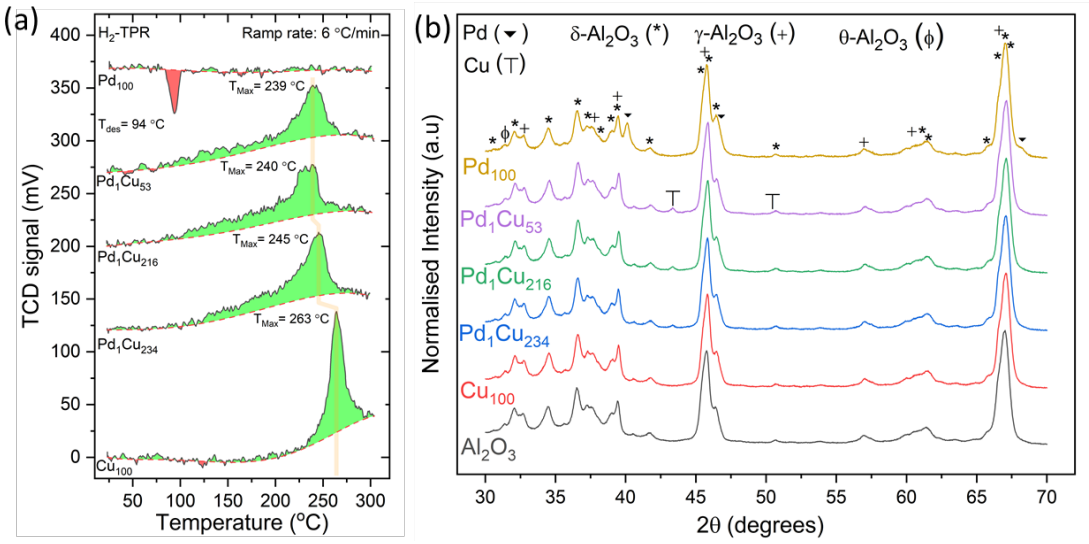

Fig. 1 (a) H_2 Temperature programmed reduction of Cu, PdCu and Pd catalysts. Gas composition was 5% H_2/ 95% N_2 v/v at 40 ml min^{-1} with a heating rate of approximately 6 °C min^{-1}. (b) XRD diffractograms of reduced ex situ Pd, Cu and PdCu species supported on Al_2O_3 catalysts and the bare support.

3.1.3 Powder X-ray Diffraction (PXRD) and Selected Area Electron Diffraction (SAED)

Fig. 1 (b) shows *ex situ* XRD diffractograms of the catalytic materials after reduction at 300 °C for 0.5 h. The diffractograms show broad but discernible reflections characteristic of nano-crystalline γ-Al_2O_3 (JCPDS card No. 29-0063) and δ-Al_2O_3 (JCPDS card No. 46-1215), and a

small impurity arising from the θ-Al_2O_3 phase (JCPDS card No. 11-0517). A quantitative examination of the diffractograms shows that the lattice parameters of the alumina phases remain unaltered (Table S1), suggesting that the copper/palladium phase onto the alumina did not significantly affect the overall morphology of the support. The spots forming rings observed in the SAED images of the catalysts (Fig. S3) suggest the support is largely polycrystalline, as amorphous materials will form more noticeable diffused rings. It should be noted that only spots relating to the γ-Al_2O_3 and δ-Al_2O_3 could be distinguished. Examining the diffractograms, the host Cu_{100}/Al_2O_3 catalyst did not show any diffraction peaks arising from the Cu phase, inferring that the Cu nanoparticles are very small, and/or lacking long-range order, leading to very broad diffraction peaks. In contrast, after galvanic replacement of the Cu with Pd atoms (PdCu catalysts), a broad Cu (111) reflection is observed at 43.4°, with an estimated lattice parameter of 3.623 Å (Table S1). The appearance of the Cu (111) reflection after Pd is incorporated can be attributed to the effect of the galvanic replacement (GR) process in the increase of the order of the Cu nanoparticles in such a way that it is detectable. This effect has been reported earlier [65], suggesting that the GR process can cause the Cu ions produced directly from GR or nanoparticle dissolution to be reduced again onto the Cu nanoparticle. Thus, increasing Cu's apparent crystallinity. On the other hand, increasing the Pd loading in the catalysts did not show any significant changes in the lattice parameters, and the absence of any Pd reflections suggests the Pd atoms have been incorporated into the Cu phase without forming detectable Pd ensembles or identifiable changes in the Cu structure. As another benchmark catalyst, the monometallic Pd_{100}/Al_2O_3 catalyst showed Pd reflections consistent with that of an FCC Pd crystal structure (JCPDS card No. 05-068). In the diffractograms, Pd (29.5° for PdO, JCPDS 41-1107) and Cu oxides (36.4° and 38.8° for Cu_2O, 05–0667 and CuO, JCPDS 45-0937, respectively) were not detected, implying the nanoparticles are predominately in their metallic state with an amorphous oxide passivation layer.

3.1.4 Scanning and Transmission Electron Microscopy (STEM/TEM)

Investigation of the Cu_{100} catalyst with STEM showed the presence of very small Cu nanoparticles with an average size of 2.7 ± 0.7 nm (Fig. 2a, Fig. S4). This is in stark contrast to our previous studies [22] where a wet impregnation synthesis gave rise to isolated and dimer copper atoms embedded onto Al_2O_3 surface. Therefore, wet impregnation typically gave a range of nanostructures, while the colloidal synthesis formed monodisperse nanoparticles ideal

for understanding the formation of single-atom alloy catalysts. Nevertheless, incorporation of low levels of Pd atoms via galvanic replacement (Pd_1Cu_{234} and Pd_1Cu_{216} catalysts) causes an insignificant difference in the nanoparticle size (Fig. 2f and **Error! Reference source not found.**). Once the Pd concentration was quadrupled (Pd_1Cu_{53} catalyst), the nanoparticles appear to grow in size to 7.0 ± 4.4 nm (Fig. 2d). Particle sizes using STEM and assuming particles are monocrystalline were compared to the integral breath and WPPM methods determined via XRD (**Error! Reference source not found.**). Particle size analysis from simple line profile analysis (integral breath method and the Scherrer equation) differed from the values obtained with the WPPM calculation and STEM data. This can be explained as a volume-weighted crystallite size average is determined using the integral method, which can overestimate crystallite size by rogue larger particles. In contrast, values calculated using the WPPM method give an area-weighted average which is influenced less by large particles. WPPM and STEM results support our observation that Cu particle size increase with a large increase Pd concentration, which is hypothesised to be attributed to the reduction of Cu ions onto the existing nanoparticles [65]. TEM images of the benchmark Pd_{100} catalyst (Fig. 2e) synthesised colloidally show that the average nanoparticle size is 5.1 nm ± 2.7 nm with the presence of larger 10 nm particles supporting the dissimilarity between the TEM and XRD particle sizes.

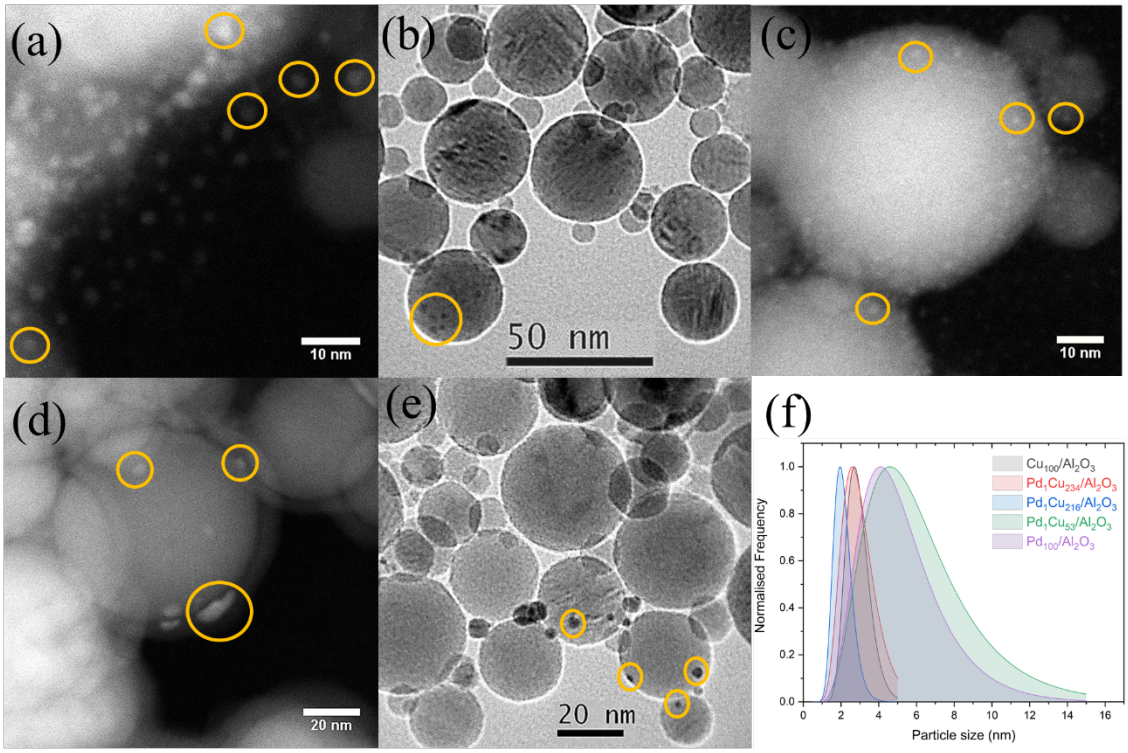

Fig. 2 STEM/TEM images of (a) Cu_{100}/Al_2O_3, (b) Pd_1Cu_{234}/Al_2O_3, (c) Pd_1Cu_{216}/Al_2O_3, (d) Pd_1Cu_{53}/Al_2O_3, (e) Pd_{100}/Al_2O_3, and (f) lognormal STEM/TEM size distributions for the catalysts reduced ex-situ at 300 ˚C for 0.5 h under flowing H_2.

3.1.5 X-ray Photoelectron Spectroscopy (XPS) and X-ray excited Auger Spectroscopy (XAES)

Fig. 3a shows X-ray photoelectron spectra of the *ex situ* reduced catalysts along with the reference spectra of Cu, CuO, Cu_2O, Pd and PdO. The characteristic Cu 2p doublet is observed with the Cu $2p_{3/2}$ transition centred at 932.8 eV (Table S2). The absence of strong shake-up satellites at 942.6 eV and 962.3 eV, shows the absence of Cu^{2+} species so, the Cu is largely in its Cu^0 or Cu^+ oxidation state due exposure to atmospheric oxygen. Minimal differences in the Cu $2p_{3/2}$ transition are observed between the catalysts. It should also be noted that the binding energies of Cu^+ and Cu^0 are very similar, making deconvolution problematic. With this in mind, the composition the Cu species were determined according to the Cu $2p_{3/2}$ and satellite peaks [66-68]. Surface compositional analysis (Table S2) shows 1-3% Cu^{2+} in the SAA catalysts with the Cu species being largely in the Cu^0 or Cu^+ state.

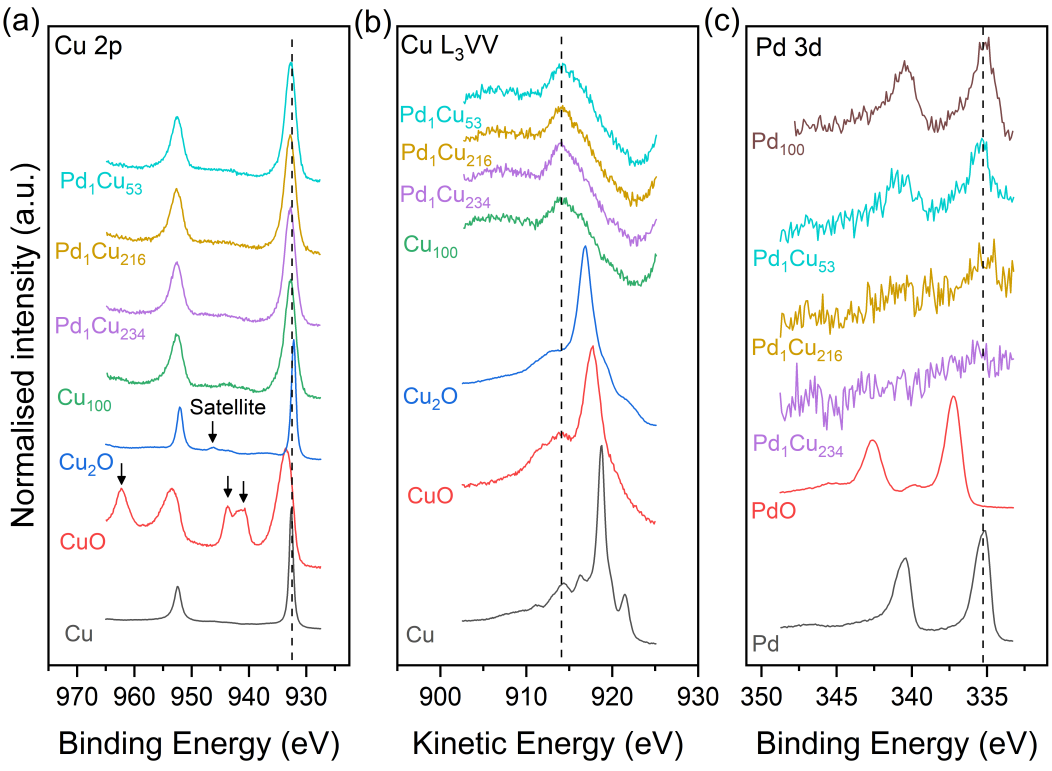

Fig. 3 High-resolution stacked XPS and XAES spectra of the (a) Cu 2p, (b) Cu L_3VV and (c) Pd 3d regions for the PdCu catalysts after being reduced ex situ at 300 °C.

The Cu L_3VV Auger transitions of the catalysts are found to be attenuated and significantly shifted to lower kinetic energies compared to the Cu_2O reference. Such observations in the shifts in the Auger transitions and the modified Auger parameter, α' are not without precedent for supported catalysts [22, 61, 69]. The modified Auger parameter is dependent on both initial and final state effects, providing an estimate of the relaxation/screening energies due to the presence of core-holes [70], while being independent of sample charging and energy calibration problems [71]. It is observed that the α' of the Cu_{100} catalyst to be 1847.4 eV, which is drastically lower than bulk Cu (α'_{bulk} = 1851.4 eV). The shift is attributed largely to the polarizability of the support [72] which can withdraw electrons from the Cu nanoparticles; reducing the ability of the Cu atoms to screen the core-hole after photoemission. It is reported that the Cu atoms in a PdCu bimetallic systems can act as electron donors to Pd atoms [73], whereby a further decrease in screening efficiency of the conduction electrons is observed by the decrease in α' with Pd introduction. Theoretically, the heterometallic Cu-Pd bond is formed by charge loss in Cu(4sp) and, to a lesser degree, Pd(4d) bands, with a rise in the population of Pd(5sp) but no change in the occupancy of the Cu(3d) band. As a result, the electronic configuration of the alloy cannot be viewed as a mere superposition of pure metals [74]. The

spectra in Fig. 3 suggest the surface oxide is most likely comprised of Cu_2O for the catalysts due to the surface composition analysis and the shift in the Cu L_3VV transition.

The Pd $3d_{5/2}$ transition of the monometallic benchmark Pd_{100}/Al_2O_3 is found at 335.1 eV consistent with that of bulk metallic Pd (335.2 eV, Table S2). In addition, PdO could not be detected/deconvoluted via fitting suggesting the Pd present is in its metallic state. A severely attenuated Pd $3d_{5/2}$ transition centered at 335.3 eV is observed for the Pd_1Cu_{53} catalyst due to the trace concentration of Pd. The slight observed shift compared to Pd_{100} catalyst correlates well with earlier literature [41, 75] due to the Pd-O-Cu interaction on the surface after the passivation of the Cu nanoparticles. A further shift of 0.19 eV with the lower Pd loaded Pd_1Cu_{216} catalyst compared to the Pd_1Cu_{53} catalyst suggests the Pd atoms have a greater O-Cu interaction suggesting a larger ratio of Pd surface atoms compared to atoms sinking into the bulk.

Fig. S5 shows the XPS derived dispersion calculations and, as mentioned earlier, it can give an insight into the location of the Cu and Pd atoms present in the catalysts. For the monometallic Cu_{100} catalyst, a dispersion value of 71.0 ± 7.1% is determined which equates to a spherical nanoparticle size of ~1.5 nm (Fig. S6). The lower equivalent nanoparticle size can be attributed to the fact that XPS can detect Cu atoms irrespective of them being present in small nanoparticles or large nanoparticles while with STEM/TEM it is difficult to distinguish very small particles from the support because of the Z-contrast. As observed in the STEM/TEM and XRD data the low replacement levels of Cu atoms with Pd atoms appear not to decrease the dispersion of the Cu phase. However, with significantly higher Pd loading (Pd_1Cu_{53} catalyst) the dispersion slightly decreases. The significantly increased Pd dispersion of the Pd_1Cu_{216} catalyst supports the idea mentioned earlier related to the positive shift of the Pd $3d_{5/2}$ transition of the Pd_1Cu_{216} compared to the Pd_1Cu_{53} catalyst, which was linked to an increased proportion of the Pd atoms sunk into the bulk of the nanoparticle for the latter.

3.1.6 X-ray Absorption Spectroscopy (XAS)

Pseudo-*in situ* and *ex situ* EXAFS (Fig. 4 and Fig. 5) suggest that Pd atoms have successfully galvanically replaced the Cu atoms on the nanoparticles while remaining atomically dispersed, confirming the formation of the single-atom catalysts. The tabulated (Table 2) first shell Pd-Cu bond lengths for the reduced Pd_1Cu_{53} and Pd_1Cu_{216} catalysts were found to be 2.562 ± 0.011 Å and 2.551 ± 0.015 Å, which coincides with a Cu-Cu bond (2.551 ± 0.054 Å).

Table 2 EXAFS model fitting of re-oxidised and reduced $PdCu/Al_2O_3$ catalysts, Pd and Cu reference foils.

Sample	Sample form	Shell	CN	R (Å)	σ^2 (Å^2) $\times 10^3$	ΔE_0 (eV)	R factor
Pd foil	-	Pd-Pd	12	2.742 ± 0.002	5.6 ± 0.4	3.70 ± 0.39	0.0163
Cu foil	-	Cu-Cu	12	2.551 ± 0.054	9.3 ± 0.8	2.96 ± 0.84	0.0270
Pd_1Cu_{53}	Re-oxidised	Pd-Cu	5.2 ± 0.9	2.563 ± 0.011	5.5 ± 1.3	0.87 ± 2.23	0.0134
Pd_1Cu_{53}	Reduced	Pd-Cu	5.4 ± 0.8	2.562 ± 0.087	5.1 ± 1.0	1.48 ± 1.73	0.0080
Pd_1Cu_{216}	Re-oxidised	Pd-O Pd-Cu	2.5 ± 1.3 2.5 ± 1.0	2.003 ± 0.044 2.564 ± 0.007	7.5 ± 5.8 4.4 ± 2.9	3.31 ± 5.89	0.0163
Pd_1Cu_{216}	Reduced	Pd-Cu	3.7 ± 0.9	2.551 ± 0.015	5.5 ± 1.7	-0.30 ± 3.08	0.0110

CN, average coordination number; R, the distance between the absorber and backscattered atoms. σ^2 multiplied by 10^3, Debye-Waller factor; ΔE_0, the photoelectron energy origin; R-factor, the closeness of fit.

The Pd atoms determined to be missing Pd-Pd (2.742 Å, Pd metal) and bulk alloyed Pd-Cu (2.63 Å, Cu_3Pd) coordination supporting theoretical calculations [39] that Pd can form a stable single-atom catalyst on Cu (111) surfaces. In addition, the sinusoidal waveform of the EXAFS in k-space (Fig. 4a) is consistent with the absence of multiple different scattering species in the measured local coordination environment [76]. Coordination numbers of the Pd-Cu shell were found to be 5.4 ± 0.8 (Pd_1Cu_{53}) and 3.7 ± 0.9 (Pd_1Cu_{216}), much lower than the typical FCC bulk and surface (111) coordination numbers of 12 and 9. This suggests the Pd atoms are incorporated on/near the surface in very small nanoparticles with dangling bonds. The Pd_1Cu_{53} catalyst has 340% more Pd compared to the Pd_1Cu_{216}. This extra Pd is accommodated throughout the nanoparticle, and therefore, significant portion of it is populating the bulk of the nanoparticle. This statement is further supported by the difference in coordination numbers of Pd as seen in Table 2. Pei et al. [48] also reported Pd-Cu bond length and coordination of 2.58 Å and 11.6 respectively for a PdCu SAA synthesised via co-impregnation. However, co-impregnation distributes Pd atoms throughout the nanoparticle while galvanic replacement selectively replaces surface atoms explaining the difference in coordination numbers since in one case Pd atoms are distributed homogeneously and the other heterogeneously.

Typically, EXAFS alone does not provide insight on whether the Pd atoms are on the surface or in the bulk since the technique gives the average local environment across the whole sample. Any attempts to determine such information will usually result in the use of highly correlated parameters producing unreliable results. The presence of Pd surface atoms is important for the increasing the hydrogen dissociation capability of the catalyst [39, 44, 46, 47]. In-situ FTIR methods exist [77] utilising CO as a surface probe molecule, but such experiments rely on an adequate signal-to-noise ratio. In this method it is crucial to determine whether the absence of bridged CO vibrational modes is due to the presence of single atoms or the lack of signal caused by the trace loading of the dopant. DFT calculations suggest Pd and Pt are stable on a Cu surface due to their relatively lower surface energies and higher deformation energies [39]. To

examine this experimentally, the samples were reduced and re-oxidised at room temperature by exposing them to atmospheric oxygen. Selectively altering the surface Pd atoms with oxidation allows to easily differentiate surface Pd species from any Pd diffused into the bulk which will be largely unaffected. Pd-O coordination is observed in the Pd_1Cu_{216} catalyst with a reduction in the Pd-Cu coordination from 3.7 to 2.5 suggesting a significant portion of the Pd atoms remain on the surface via selective oxidation. In contrast, the Pd_1Cu_{53} catalysts seem to be largely unaffected by the surface oxidation (a slight drop in Pd-Cu coordination of 0.2), suggesting a significant portion of the atoms have diffused below the topmost layer of the nanoparticle, supported by our XPS findings. We propose this phenomenon is due to the increased population of the Cu surface with Pd atoms promoting diffusion into the bulk. It should be noted also that this method is not entirely ideal, as in actual reaction conditions adsorbed hydrogen can stabilise surface Pd atoms bringing more atoms up to the surface [39, 78, 79]. The Pd-O bond length of the Pd_1Cu_{216} catalyst was found to be 2.003 ± 0.044 Å, which is reminiscent of bulk PdO (2.01 Å). This indicates the surface Pd atoms can distort the Cu oxidised phase, as the Cu-O bond lengths are 1.88 Å and 1.96 Å for Cu_2O and CuO, respectively. Additionally, an increase in the Pd-Cu bond lengths can be observed with copper oxidation, the largest increase been detected in the Pd_1Cu_{216} catalyst. This can be correlated to the increased perturbation of the underlying Cu lattice of the nanoparticles by the oxide layer.

In Fig. S7 and Table S3, we compare the XANES spectra and Pd K-edge energy. After reduction, the Pd atoms are slightly negatively charged [48] (discussed previously) while after oxidation the edge is shifted to higher energies due to oxygen withdrawing electron density from its surrounding atoms. The XANES also suggest the Pd species are in their zeroth oxidation state due to the presence of the 2nd peak after the edge appearing only after reduction for the Pd_1Cu_{216} catalyst [80].

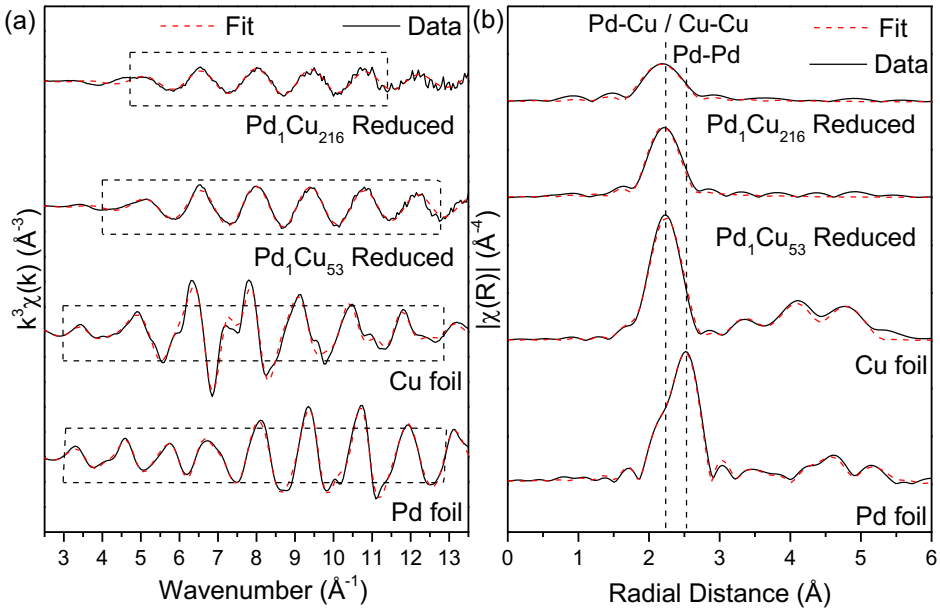

Fig. 4 (a) Pseudo-in-situ EXAFS spectra in k-space (k-weight = 3) and (b) R-space (k-weight = 3) for PdCu/Al_2O_3 catalysts (reduced ex-situ and placed an gas-tight cell via a glovebox to prevent oxidation) along with Pd and Cu reference foils. Dashed-lined rectangles indicate k ranges over which the data were then Fourier transformed and analysed.

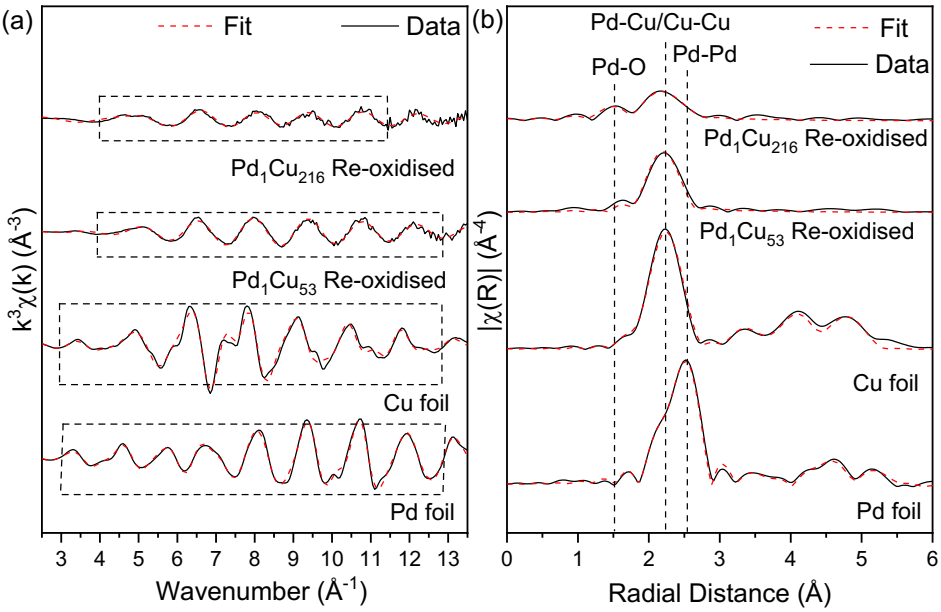

Fig. 5 (a) EXAFS spectra in k-space (k-weight = 3) and (b) R-space (k-weight = 3) for PdCu/Al_2O_3 catalysts (reduced ex-situ) along with Pd and Cu reference foils. Dashed-lined rectangles indicate k ranges over which the data were then Fourier transformed and analysed.

3.2 Catalytic testing

Mild reaction conditions were chosen as low temperatures and pressures are critical for the future of sustainable chemistry, especially for batch reactions. Additionally, the use of higher

temperatures is known for reducing the selectivity away from furfuryl alcohol and towards decarbonylation reactions [4]. The catalytic data reveal that adding trace amounts of Pd to the Cu nanoparticles has significantly improved the hydrogenation of furfural at 50 °C with 1.5 bar of hydrogen (Table 3). The Pd/Cu catalysts show higher activity than Cu and higher selectivity than Pd. In the absence of any solid catalyst, neither decarbonylation nor hydrogenation reactions were observed. The parent Al_2O_3 support was also found to be inactive towards the hydrogenation of furfural, favouring mostly the acetalization of furfural with methanol, with negligible conversion (Table S4). The major product observed for all catalysts were furfuryl alcohol (FA) while other side products were 2-furaldehyde dimethyl acetal (FDMA, MS spectrum in Fig. S8) and tetrahydrofurfuryl alcohol (THFA). It should be noted, the lower carbon balance of the Pd_{100} catalyst is attributed to unquantifiable decomposition/ether products [81].

Table 3 Summary of catalytic data for the hydrogenation of furfural using Pd/Cu catalysts. Reaction conditions: 7 h, 50 °C, 1.5 bar, 600 rpm, and 30 mg of catalyst. Catalyst, reactant and solvent weight percentages are 0.38%, 0.24% and 99.20%, respectively.

Catalyst	Conversion (%)	FA S (%)	FDMA S (%)	THFA S (%)	Carbon Balance S (%)
Cu_{100}	23.1 ± 1.2	98.2 ± 4.9	1.8 ± 0.1	0.0	98.1 ± 4.9
Pd_1Cu_{234}	30.3 ± 1.5	97.9 ± 4.9	2.1 ± 0.1	0.0	96.6 ± 4.8
Pd_1Cu_{216}	40.1 ± 2.0	99.1 ± 5.0	0.9 ± 0.1	0.0	96.9 ± 4.8
Pd_1Cu_{53}	38.2 ± 2.9	98.0 ± 4.9	2.0 ± 0.1	0.0	96.2 ± 4.9
Pd_{100}	60.4 ± 3.0	89.7 ± 4.4	2.8 ± 0.2	7.5 ± 0.4	84.4 ± 4.3

Fig. 6a indicates an induction period of approximately 1 h where the Cu-based catalysts are inactive in terms of conversion. This behaviour is thought to be due to the limited catalytically available adsorbed hydrogen at the start of the reaction either through the formation of surface oxide (from O_2 contamination) or Cu's inability to adequately chemisorb hydrogen. However, the presence of Pd with the SAA catalysts seems to lessen its effects. This is in stark contrast to the monometallic Pd_{100} catalyst which lacks any such induction period due to its increased resistance to oxidation, higher reducibility and likely also due to the extended Pd surface to store hydrogen as β-hydride species during the *in situ* reduction treatment [14, 61-63]. However, the Cu rich catalyst's low activity is offset by its high selectivity. The increased selectivity is due to furfural binding to the surface via the lone pairs in the carbonyl functional group (E_{ads} = -0.91 eV, [51]), promoting hydrogenation of the C ═ O bond instead of the C ═ C bond [82]. Pd surfaces are very reactive, allowing η^2(C, O)-aldehyde bonding modes (E_{ads} =

-1.91 eV, [83]), in which both O and C are bound [4, 83, 84]. As a result, unidentified decarboxylation/ethers products are promoted, creating higher discrepancy in the carbon balance (Fig 6b), and the THFA formation is also favoured. The lower selectivity of the Pd_{100} catalysts towards furfuryl alcohol could be associated with the presence of larger Pd flat surfaces which can lead to more ring hydrogenation products (THFA). Such behaviour has been reported for Pd catalysts by Li *et al.* [4]. Such sides products observed for Pd catalysts are not observed with the SAA catalysts since it requires extended Pd surfaces for such side reactions to occur, so the selectivity is provided by the Cu surfaces. This is also supported by previous DFT studies [52], where the Cu in PdCu alloys reduce the stability of the η^2(C, O)-aldehyde adsorption present on Pd (111) indicated by the decrease in the heat of adsorption from 55.4 kJ/mol to 9.6 kJ/mol, thus the rate of decarbonylation reduced and hydrogenation is promoted. However, in the case of bimetallic PdAg alloys [29], Ag addition was reported to reduce the adsorption strength of furfuryl alcohol from -1.44 eV to -1.01 eV, reducing its further hydrogenation, thus improving the selectivity. Isolated Pd atoms are also reported to act as entry sites for hydrogen to dissociate and adsorb after which they H_{ads} spill over onto the Cu surface [39, 41, 44, 46, 47, 85-87] where they react with the adsorbed substrate.

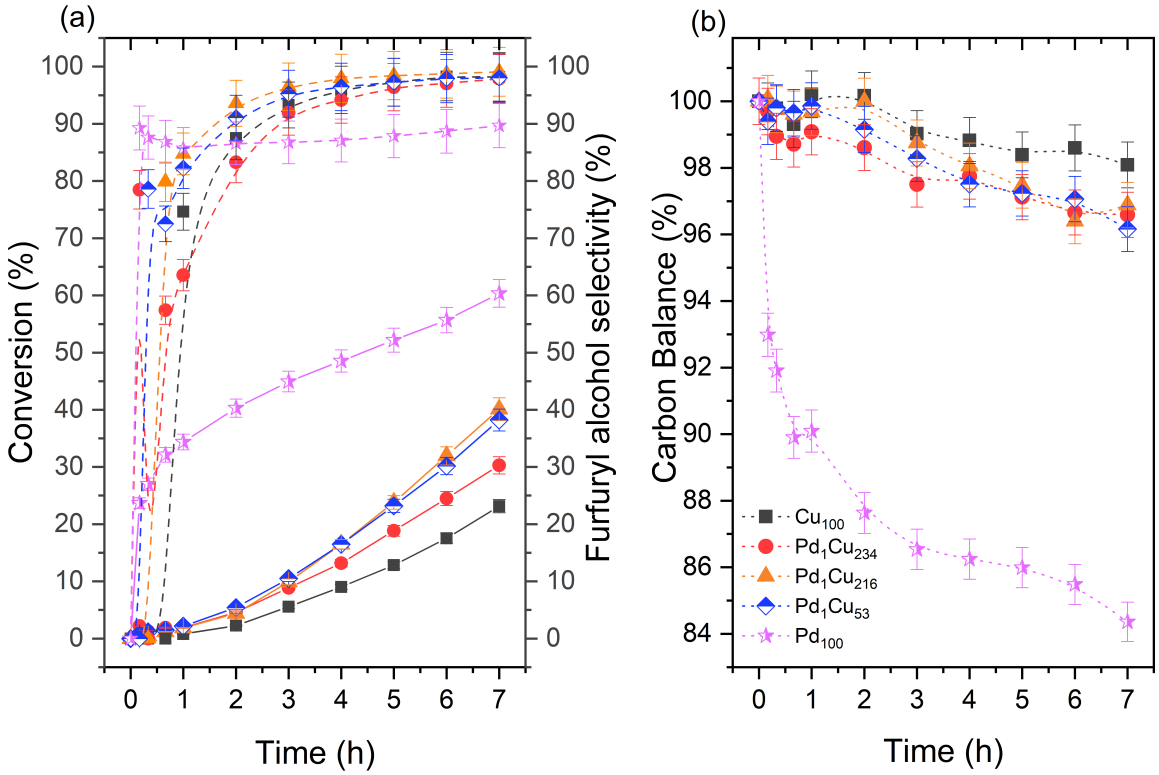

Fig. 6 The reaction profiles of (a) furfural conversion, selectivity and (b) carbon balance. Reaction conditions: 7 h, 50 °C, 1.5 bar of H_2, 600 rpm, 30 mg of catalyst. Solid lines, dashed, and dotted lines represent conversion, selectivity, and carbon balance, respectively.

Fig. 7a demonstrates the initial rates of furfural consumption for the PdCu SAA and the monometallic catalysts normalized for the Pd and the Cu metal content. This is of particular importance as the mechanistic action of the two metals in the reaction is most likely different with Pd being responsible mostly for the dissociative adsorption of hydrogen on the catalyst surface while Cu providing the surface upon which the hydrogenation reaction takes place [38, 41, 44, 47]. Clearly when the initial rates of the PdCu SAA are normalized for the Pd metal content, they appear to outperform the monometallic Pd catalyst as the amount of Pd present in these catalysts is significantly lower. Particularly, the Pd_1Cu_{216} catalyst demonstrates an eleven-fold increase in activity compared to the monometallic Pd_{100} catalyst due to the aforementioned difference in Pd content. More interestingly, improvements are also observed over the Cu_{100} catalyst, showing that trace amounts of Pd atoms can augment the catalytic surface by promoting hydrogen adsorption. The improvement in activity with Pd loading has a diminishing return, with the Pd_1Cu_{216} catalyst being the superior atom-efficient catalyst. It is proposed this trend is due to the Pd atoms being inaccessible to be used as hydrogen dissociation entry sites since the EXAFS suggests a significant portion of Pd atoms have diffused under the surface of the nanoparticle. Analysing the furfuryl alcohol production profile

normalised to the total metal (Fig. 7b) shows that the atomically dispersed Pd_1Cu_{216} catalyst can improve the performance of the Cu host surface to that of the benchmark monometallic Pd_{100} catalyst. While it can be clearly seen that both systems follow drastically different reaction mechanisms, explained earlier through the different reactant binding modes/hydrogen storage capability of Pd and Cu majority surfaces.

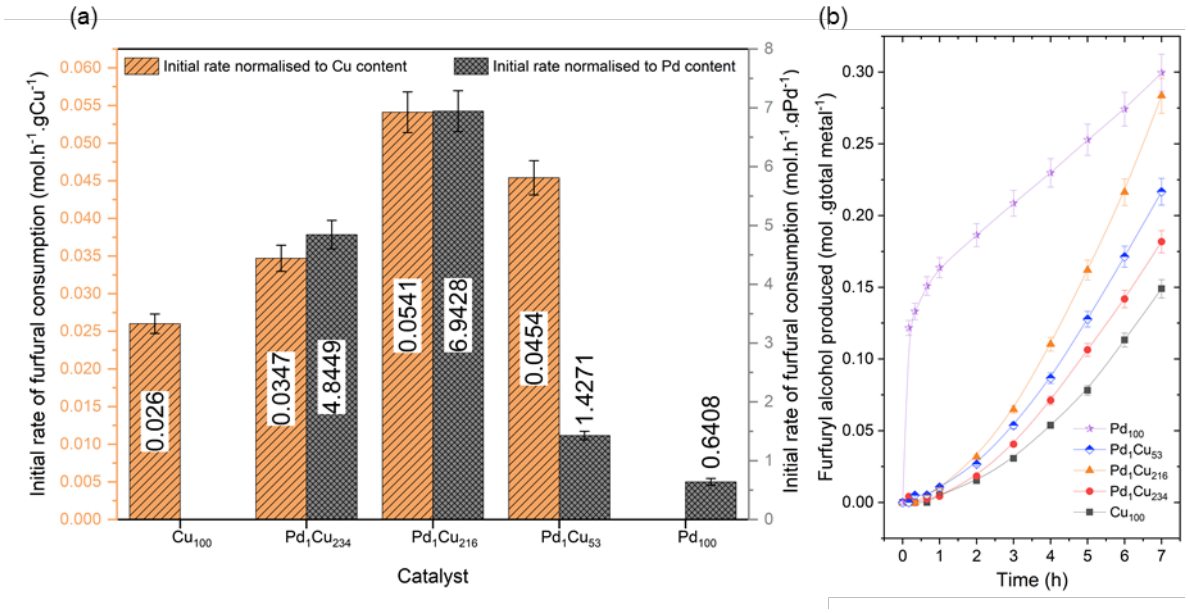

Fig. 7 (a) Initial rate of the furfural consumption normalised to Cu and Pd content. The initial rate was determined after the induction period for the Cu-based catalysts. (b) Furfuryl alcohol production over time normalised to the total metal. Reaction conditions: 7 h, 50 °C, 1.5 bar of H_2, 600 rpm, 30 mg of catalyst.

To determine if the active sites are better instead of the contributing effect of increased active sites due to the higher dispersion of the catalysts, the turnover frequency (TOF) was determined in Fig. 8. The TOF clearly shows that the introduction of the atomically dispersed Pd atoms increases the catalytic activity of the surface Cu sites with the optimal Pd_1Cu_{216} SAA catalyst increasing Cu TOFs by ~85%. Further increasing the Pd loading with the Pd_1Cu_{53} comes with diminishing returns as the TOFs are not seen to increase which is also observed in the normalised initial rates (Fig.). When comparing TOFs of the monometallic Pd_{100} catalyst to a SAA catalyst shows that the atomically dispersed Pd sites are ~173% more catalytically active than the typically equivalent surface sites found on Pd nanoparticles. Supporting the previous data, it can be noticed that initially as the Pd loading is increased the activity of the Pd sites also increases to a maximum TOF of 813 ± 81 h^{-1}. Further drastic increases in the Pd loading with the Pd_1Cu_{53} catalyst appears to begin to render the Pd sites less effective, possibly changing their properties to be more like that of a monometallic Pd catalyst. It should be noted

that due to the inability to determine the Pd dispersion for the Pd_1Cu_{234} catalyst (lack of Pd 3d signal) it was assumed to be 100% for this TOF calculation. For comparison Fig. S9 shows the TOF calculation for all the catalysts using the total metal sites (both Cu and Pd). Interestingly the TOF values in this for the SAA catalysts show again a significant improvement compared to the monometallic Cu catalyst. As expected, in this comparison the Pd_{100} catalyst showed the highest TOF values due to its high content of Pd.

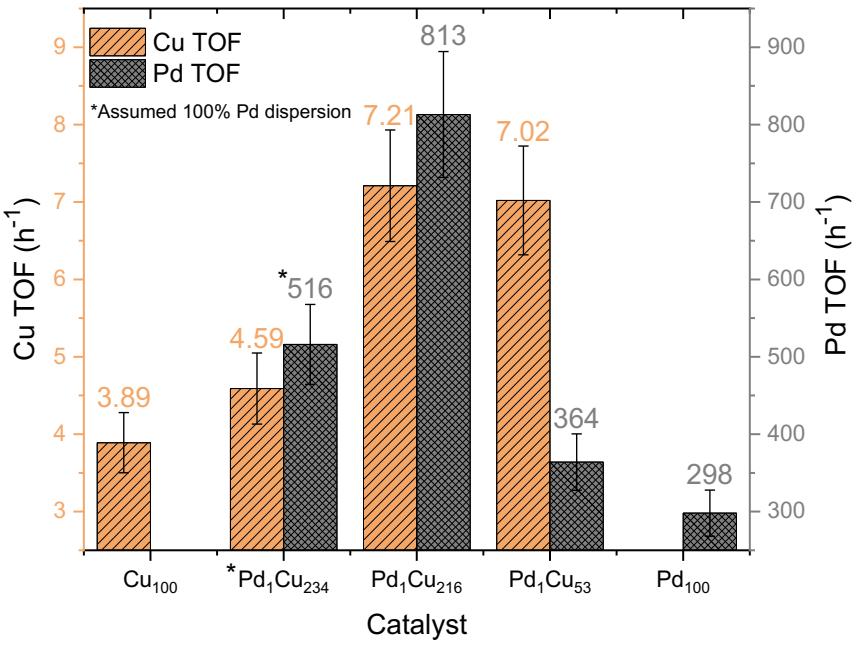

Fig. 8 Turnover frequency of both Cu and Pd surface atoms for the catalysts determined from the XPS calculated dispersion. Reaction conditions: 7 h, 50 °C, 1.5 bar of H_2, 600 rpm, 30 mg of catalyst.

Fig. 9 shows the produced furfuryl alcohol/metal mole ratio per hour (Equation 12 in supplementary information) under mild to moderate reaction temperatures and pressures. The catalysts synthesised in this work and those reported in the literature are compared. Table S5 gives the relevant conditions of operation that the experiments from literature were performed. The advantages of comparing the furfuryl alcohol mole ratio/metal per hour are that all the active metal content, yield, and reaction time are considered quantifying the best selective atom efficient catalysts. Comparing the monometallic Cu_{100}/Al_2O_3 to the industrial used Cu-Cr [88] shows the Cu-Cr catalyst is 38% more active but, requires higher temperatures and pressures of 110 °C and 10 bar of hydrogen. The optimal atom efficient catalyst under mild conditions

(90 °C, 1 bar) reported in the literature is a Pd_1/C_3N_4 single-atom catalyst [89] with a mole ratio of 158 h^{-1} while at more moderate conditions (120 °C, 6 bar) it is a Pd-Cu/C [90] catalyst with values of 289 h^{-1}. The single-atom alloy catalysts synthesised in this work is shown to make the most efficient use of the precious metal atoms when compared against the literature (Pd_1Cu_{216} = 601 h^{-1}) demonstrating the surface replacement of Cu atoms with Pd can create superior atom efficient catalysts.

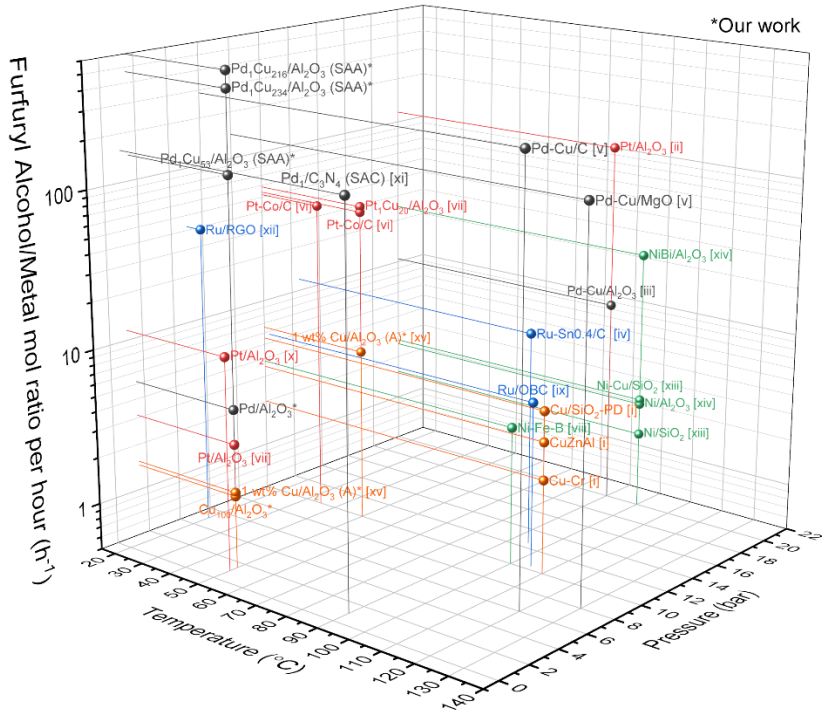

Fig. 9 Furfuryl alcohol/metal mole ratio per hour of catalysts from this work and various catalysts found in the literature under low to moderate conditions (<140 °C and <20 bar). Square bracketed Roman numerals [i], [ii], [iii], [iv], [v], [vi], [vii], [viii], [ix], [x], [xi], [xii], [xiii], [xiv] and [xv] represent references [91], [92], [14], [20], [90], [15], [6], [93], [94], [2], [89], [95], [96], [97] and [22], respectively. Log_{10} scale is used for the furfuryl alcohol/metal ratio per hour z axis and the colour of the spheres represents which metal is used for the calculation. Pd, Pt, Ru, Ni and Cu represent sphere colours dark grey, red, blue, green, and orange, respectively.

3.2.1 Spent catalyst characterisation and recycling experiments

Comparing the XPS spectra of the spent and fresh Pd_1Cu_{216} catalysts (Fig. S10) shows that after recovery, the spent material is significantly oxidised to CuO which is observed by the strong shake-up satellites and the shift of the Cu $2p_{3/2}$ transition by +0.82 eV. Note that the surface copper in the fresh catalyst appears to be in the metallic state after pre-treatment with hydrogen. However, the recovery of the spent catalyst involves centrifugation, washes and drying in air at 60 °C, causing the oxidation of the copper surface at the time of the analysis. Surface compositional analysis in Table S5 confirms the Cu species are largely in their Cu^{2+} oxidation state (77.5%). As observed for the unused catalyst, the modified Auger parameter is found noticeably lower than bulk Cu (α'_{bulk} = 1851.38 eV) or that of bulk CuO (α'_{CuO} =

1851.40) for the spent material. Though, the α' is also shifted by +0.63 eV, like that of Cu_2O, though due the satellite structure/compositional analysis it can be presumed the shift arises from the presence of CuO while the overall negative shift of the parameter is due to Cu's close contact to the polarisable support. However, the XPS calculated Cu dispersion values show that there may be some loss in Cu dispersion through nanoparticle sintering.

The recyclability of the optimal PdCu SAA catalyst was investigated. The catalysts were recovered after the reaction via centrifugation followed by washing with methanol. Once dried at 60 °C overnight, the spent materials were weighed and retested. Due to losses of catalyst during sampling and recovery, a reaction cycle at 75% of the original scale was used in the spent catalyst run to keep weight percentages of catalyst, reactant and solvent consistent with the fresh catalyst run. Table 4 shows that the conversion and selectivity of the catalyst was within error minimally affected after reuse. Which is consistent with the ICP-OES analysis of the filtered supernatant fluid as the elemental analysis ruled out Cu leaching.

Table 4 Furfural hydrogenation over the recycled catalysts. Reaction conditions: 7 h, 50 °C, 1.5 bar of H_2 and 600 rpm.

Catalyst	Conversion (%)	FA S (%)	FDMA S (%)	THFA S (%)	Carbon Balance S (%)
Pd_1Cu_{216}[1]	40.1 ± 2.0	99.1 ± 5.0	0.9 ± 0.1	0.0	96.9 ± 4.8
Pd_1Cu_{216}[2]	37.5 ± 1.9	97.4 ± 4.9	2.6 ± 0.1	0.0	97.0 ± 4.9

Superscripts 1 and 2 indicate the catalyst cycle of testing.

4 Conclusions

A series of bimetallic PdCu catalysts were tested for the selective hydrogenation of furfural under mild conditions. The catalyst morphology and electronic properties were thoroughly studied utilising XRD, XPS, STEM, EXAFS, XANES, TPR and ICP-OES. Catalyst characterisation confirms that Pd atoms were atomically dispersed on the host copper nanoparticle surface, confirming the formation of a single atom catalyst. With the combination of pseudo-*in situ* and *ex situ* EXAFS suggests that as the Pd loading increases, Pd atoms diffuse into the bulk reducing their catalytic effectiveness. The augmentation of the copper surface with trace amounts of Pd (0.0067 wt%) was found to improve the host Cu catalyst to that of a Pd catalyst in terms of normalised furfuryl alcohol production. Also, when compared to the Cu_{100} catalyst 1.7 and 1.9 times in performance is observed in the conversion and Cu TOFs, respectively. While the largest benefit of the SAA catalysts is based on atom efficiency, improvements are also observed in yields such that the Pd_1Cu_{216} (Y% = 36.9 ± 1.8) catalyst performs almost as well as the Pd_{100} (Y% = 40.4 ± 2.0) benchmark catalyst and considerable better than the Cu_{100} catalyst (Y% = 20.9 ± 1.0). The synthesised atom efficient catalysts retain

Cu's high selectivity attributed to the incredible control of the Pd active sites since they are isolated, which eliminates competitive side-reactions that require more than one Pd neighbouring atoms. This work also shows the formation of a single atom alloy catalyst is not enough, but such isolated atoms need to be present on the surface to be ensure maximum efficiency. Finally, when compared against the literature, it was found that these materials are, to the best of our knowledge, the most competitive atom efficient catalysts implemented for the selective hydrogenation of furfural to furfuryl alcohol, especially when using both low H_2 pressure and reaction temperature.

Acknowledgements

The authors wish to acknowledge the Diamond Light Source and the UK Catalysis Hub for provision of beamtime (proposal number SP19850-5 and SP19850-6). Also specifically acknowledge Dr Nitya Ramanan and Dr June Callison for their help with EXAFS experiments. MJI acknowledges the award of a PhD scholarship from Aston University. The authors also acknowledge the Energy Research Accelerator (ERA) for the funding of equipment used in this work. GK acknowledges funding from EPSRC (EP/M005186/2). MJT acknowledges funding through the THYME project (UKRI, Research England). The authors wish to thank M. Kollia of the Laboratory of Electron Microscopy and Microanalysis (L.E.M.M.) at University of Patras for TEM images. ST and GK acknowledge funding by grant no. 80643 provided by the ″K. Karatheodory″, University of Patras.

References

[1] R. Garnaut, L. Song, Rapid industrialization and market for energy and minerals: China in the East Asian context, Front. Econ. China, 1 (2006) 373-394.
[2] M.J. Taylor, L.J. Durndell, M.A. Isaacs, C.M.A. Parlett, K. Wilson, A.F. Lee, G. Kyriakou, Highly selective hydrogenation of furfural over supported Pt nanoparticles under mild conditions, Appl. Catal. B, 180 (2016) 580-585.
[3] M.J. Biddy, C. Scarlata, C. Kinchin, Chemicals from Biomass: A Market Assessment of Bioproducts with Near-Term Potential, ; National Renewable Energy Lab. (NREL), Golden, CO (United States), 2016, pp. Medium: ED; Size: 131 p.
[4] X. Li, P. Jia, T. Wang, Furfural: A Promising Platform Compound for Sustainable Production of C4 and C5 Chemicals, ACS Catal., 6 (2016) 7621-7640.
[5] M. Carrier, R. Fournet, B. Sirjean, S. Amsbury, Y.B. Alfonso, P.-Y. Pontalier, A. Bridgwater, Fast Pyrolysis of Hemicelluloses into Short-Chain Acids: An Investigation on Concerted Mechanisms, Energy & Fuels, 34 (2020) 14232-14248.
[6] M.J. Taylor, S.K. Beaumont, M.J. Islam, S. Tsatsos, C.A.M. Parlett, M.A. Issacs, G. Kyriakou, Atom efficient PtCu bimetallic catalysts and ultra dilute alloys for the selective hydrogenation of furfural, Appl. Catal. B, 284 (2021) 119737.

[7] C. del Pozo, F. Rego, Y. Yang, N. Puy, J. Bartrolí, E. Fàbregas, A.V. Bridgwater, Converting coffee silverskin to value-added products by a slow pyrolysis-based biorefinery process, Fuel Process. Technol., 214 (2021) 106708.
[8] K. Yan, G. Wu, T. Lafleur, C. Jarvis, Production, properties and catalytic hydrogenation of furfural to fuel additives and value-added chemicals, Renew. Sustain. Energy Rev., 38 (2014) 663-676.
[9] F. Ullmann, Ullmann's encyclopedia of industrial chemistry, 7th ed., Wiley-VCH ;, Weinheim, Germany :, 2009.
[10] J.A. Brydson, 28 - Furan Resins, in: J.A. Brydson (Ed.) Plastics Materials (Seventh Edition), Butterworth-Heinemann, Oxford, 1999, pp. 810-813.
[11] D. Liu, D. Zemlyanov, T. Wu, R.J. Lobo-Lapidus, J.A. Dumesic, J.T. Miller, C.L. Marshall, Deactivation mechanistic studies of copper chromite catalyst for selective hydrogenation of 2-furfuraldehyde, J. Catal., 299 (2013) 336-345.
[12] R. Rao, A. Dandekar, R.T.K. Baker, M.A. Vannice, Properties of Copper Chromite Catalysts in Hydrogenation Reactions, J. Catal., 171 (1997) 406-419.
[13] H. Adkins, R. Connor, The catalytic hydrogenation of organic compounds over copper chromite, J. Am. Chem. Soc., 53 (1931) 1091-1095.
[14] M. Lesiak, M. Binczarski, S. Karski, W. Maniukiewicz, J. Rogowski, E. Szubiakiewicz, J. Berlowska, P. Dziugan, I. Witońska, Hydrogenation of furfural over Pd–Cu/Al_2O_3 catalysts. The role of interaction between palladium and copper on determining catalytic properties, J. Mol. Catal. A: Chem., 395 (2014) 337-348.
[15] M.G. Dohade, P.L. Dhepe, Efficient hydrogenation of concentrated aqueous furfural solutions into furfuryl alcohol under ambient conditions in presence of PtCo bimetallic catalyst, Green Chem., 19 (2017) 1144-1154.
[16] Y. Nakagawa, K. Takada, M. Tamura, K. Tomishige, Total Hydrogenation of Furfural and 5-Hydroxymethylfurfural over Supported Pd–Ir Alloy Catalyst, ACS Catal., 4 (2014) 2718-2726.
[17] S. Srivastava, P. Mohanty, J.K. Parikh, A.K. Dalai, S.S. Amritphale, A.K. Khare, Cr-free Co–Cu/SBA-15 catalysts for hydrogenation of biomass-derived α-, β-unsaturated aldehyde to alcohol, Chinese J. Catal., 36 (2015) 933-942.
[18] J. Wu, G. Gao, J. Li, P. Sun, X. Long, F. Li, Efficient and versatile CuNi alloy nanocatalysts for the highly selective hydrogenation of furfural, Appl. Catal. B, 203 (2017) 227-236.
[19] A.B. Merlo, V. Vetere, J.M. Ramallo-López, F.G. Requejo, M.L. Casella, Liquid-phase furfural hydrogenation employing silica-supported PtSn and PtGe catalysts prepared using surface organometallic chemistry on metals techniques, React. Kinet. Mech. Catal., 104 (2011) 467-482.
[20] J.J. Musci, A.B. Merlo, M.L. Casella, Aqueous phase hydrogenation of furfural using carbon-supported Ru and RuSn catalysts, Catal. Today, 296 (2017) 43-50.
[21] S. Liu, Y. Amada, M. Tamura, Y. Nakagawa, K. Tomishige, One-pot selective conversion of furfural into 1,5-pentanediol over a Pd-added Ir-ReOx/SiO_2 bifunctional catalyst, Green Chem., 16 (2014) 617-626.
[22] M.J. Islam, M. Granollers Mesa, A. Osatiashtiani, M.J. Taylor, J.C. Manayil, C.M.A. Parlett, M.A. Isaacs, G. Kyriakou, The effect of metal precursor on copper phase dispersion and nanoparticle formation for the catalytic transformations of furfural, Appl. Catal. B, 273 (2020) 119062.
[23] M. Luneau, J.S. Lim, D.A. Patel, E.C.H. Sykes, C.M. Friend, P. Sautet, Guidelines to Achieving High Selectivity for the Hydrogenation of α,β-Unsaturated Aldehydes with Bimetallic and Dilute Alloy Catalysts: A Review, Chem. Rev., 120 (2020) 12834-12872.

[24] R. Šivec, B. Likozar, M. Grilc, Surface kinetics and transport phenomena modelling for furfural hydrotreatment over Pd/C in isopropanol and tetrahydrofuran, Appl. Surf. Sci., 541 (2021) 148485.
[25] S. Gyergyek, A. Kocjan, M. Grilc, B. Likozar, B. Hočevar, D. Makovec, A hierarchical Ru-bearing alumina/magnetic iron-oxide composite for the magnetically heated hydrogenation of furfural, Green Chem., 22 (2020) 5978-5983.
[26] K.L. MacIntosh, S.K. Beaumont, Nickel-Catalysed Vapour-Phase Hydrogenation of Furfural, Insights into Reactivity and Deactivation, Top. Catal., 63 (2020) 1446-1462.
[27] S. Tsatsos, S. Ladas, G. Kyriakou, Electronic Properties and Reactivity of Furfural on a Model Pt(111) Catalytic Surface, J. Phys. Chem. C, 124 (2020) 26268-26278.
[28] A. Kojčinović, Ž. Kovačič, M. Huš, B. Likozar, M. Grilc, Furfural hydrogenation, hydrodeoxygenation and etherification over MoO2 and MoO3: A combined experimental and theoretical study, Appl. Surf. Sci., 543 (2021) 148836.
[29] Z.-L. Wu, J. Wang, S. Wang, Y.-X. Zhang, G.-Y. Bai, L. Ricardez-Sandoval, G.-C. Wang, B. Zhao, Controllable chemoselective hydrogenation of furfural by PdAg/C bimetallic catalysts under ambient operating conditions: an interesting Ag switch, Green Chem., 22 (2020) 1432-1442.
[30] H. Ishikawa, M. Sheng, A. Nakata, K. Nakajima, S. Yamazoe, J. Yamasaki, S. Yamaguchi, T. Mizugaki, T. Mitsudome, Air-Stable and Reusable Cobalt Phosphide Nanoalloy Catalyst for Selective Hydrogenation of Furfural Derivatives, ACS Catal., 11 (2021) 750-757.
[31] J.M. Thomas, R. Raja, Mono-, Bi- and Multifunctional Single-Sites: Exploring the Interface Between Heterogeneous and Homogeneous Catalysis, Top. Catal., 53 (2010) 848-858.
[32] J.M. Thomas, Z. Saghi, P.L. Gai, Can a Single Atom Serve as the Active Site in Some Heterogeneous Catalysts?, Top. Catal., 54 (2011) 588-594.
[33] S.L. Wegener, T.J. Marks, P.C. Stair, Design Strategies for the Molecular Level Synthesis of Supported Catalysts, Acc. Chem. Res., 45 (2012) 206-214.
[34] A. Bruix, Y. Lykhach, I. Matolínová, A. Neitzel, T. Skála, N. Tsud, M. Vorokhta, V. Stetsovych, K. Ševčíková, J. Mysliveček, R. Fiala, M. Václavů, K.C. Prince, S. Bruyère, V. Potin, F. Illas, V. Matolín, J. Libuda, K.M. Neyman, Maximum Noble-Metal Efficiency in Catalytic Materials: Atomically Dispersed Surface Platinum, Angew. Chem. Int. Ed., 53 (2014) 10525-10530.
[35] Q. Fu, H. Saltsburg, M. Flytzani-Stephanopoulos, Active Nonmetallic Au and Pt Species on Ceria-Based Water-Gas Shift Catalysts, Science, 301 (2003) 935-938.
[36] J.M. Thomas, An Exceptionally Active Catalyst for Generating Hydrogen from Water, Angew. Chem. Int. Ed., 50 (2011) 49-50.
[37] M. Flytzani-Stephanopoulos, Gold Atoms Stabilized on Various Supports Catalyze the Water–Gas Shift Reaction, Acc. Chem. Res., 47 (2014) 783-792.
[38] F.R. Lucci, J. Liu, M.D. Marcinkowski, M. Yang, L.F. Allard, M. Flytzani-Stephanopoulos, E.C.H. Sykes, Selective hydrogenation of 1,3-butadiene on platinum–copper alloys at the single-atom limit, Nat. Commun., 6 (2015) 8550.
[39] Q. Fu, Y. Luo, Catalytic Activity of Single Transition-Metal Atom Doped in Cu(111) Surface for Heterogeneous Hydrogenation, J. Phys. Chem. C, 117 (2013) 14618-14624.
[40] J. Jones, H. Xiong, A.T. DeLaRiva, E.J. Peterson, H. Pham, S.R. Challa, G. Qi, S. Oh, M.H. Wiebenga, X.I. Pereira Hernández, Y. Wang, A.K. Datye, Thermally stable single-atom platinum-on-ceria catalysts via atom trapping, Science, 353 (2016) 150.
[41] M.B. Boucher, B. Zugic, G. Cladaras, J. Kammert, M.D. Marcinkowski, T.J. Lawton, E.C. Sykes, M. Flytzani-Stephanopoulos, Single atom alloy surface analogs in Pd0.18Cu15 nanoparticles for selective hydrogenation reactions, Phys. Chem. Chem. Phys., 15 (2013) 12187-12196.

[42] L. Kuai, Z. Chen, S. Liu, E. Kan, N. Yu, Y. Ren, C. Fang, X. Li, Y. Li, B. Geng, Titania supported synergistic palladium single atoms and nanoparticles for room temperature ketone and aldehydes hydrogenation, Nat. Commun., 11 (2020) 48.
[43] T. Ishida, T. Honma, K. Nakada, H. Murayama, T. Mamba, K. Kume, Y. Izawa, M. Utsunomiya, M. Tokunaga, Pd-catalyzed decarbonylation of furfural: Elucidation of support effect on Pd size and catalytic activity using in-situ XAFS, J. Catal., 374 (2019) 320-327.
[44] G. Kyriakou, M.B. Boucher, A.D. Jewell, E.A. Lewis, T.J. Lawton, A.E. Baber, H.L. Tierney, M. Flytzani-Stephanopoulos, E.C. Sykes, Isolated metal atom geometries as a strategy for selective heterogeneous hydrogenations, Science, 335 (2012) 1209-1212.
[45] H. Wei, X. Liu, A. Wang, L. Zhang, B. Qiao, X. Yang, Y. Huang, S. Miao, J. Liu, T. Zhang, FeOx-supported platinum single-atom and pseudo-single-atom catalysts for chemoselective hydrogenation of functionalized nitroarenes, Nat. Commun., 5 (2014) 5634.
[46] G. Kyriakou, E.R.M. Davidson, G. Peng, L.T. Roling, S. Singh, M.B. Boucher, M.D. Marcinkowski, M. Mavrikakis, A. Michaelides, E.C.H. Sykes, Significant Quantum Effects in Hydrogen Activation, ACS Nano, 8 (2014) 4827-4835.
[47] H.L. Tierney, A.E. Baber, J.R. Kitchin, E.C.H. Sykes, Hydrogen Dissociation and Spillover on Individual Isolated Palladium Atoms, Phys. Rev. Lett., 103 (2009) 246102.
[48] G.X. Pei, X.Y. Liu, X. Yang, L. Zhang, A. Wang, L. Li, H. Wang, X. Wang, T. Zhang, Performance of Cu-Alloyed Pd Single-Atom Catalyst for Semihydrogenation of Acetylene under Simulated Front-End Conditions, ACS Catal., 7 (2017) 1491-1500.
[49] J. Liu, J. Shan, F.R. Lucci, S. Cao, E.C.H. Sykes, M. Flytzani-Stephanopoulos, Palladium–gold single atom alloy catalysts for liquid phase selective hydrogenation of 1-hexyne, Catal. Sci. Technol., 7 (2017) 4276-4284.
[50] R. Mariscal, P. Maireles-Torres, M. Ojeda, I. Sadaba, M. Lopez Granados, Furfural: a renewable and versatile platform molecule for the synthesis of chemicals and fuels, Energy Environ. Sci., 9 (2016) 1144-1189.
[51] Y. Shi, Y. Zhu, Y. Yang, Y.-W. Li, H. Jiao, Exploring Furfural Catalytic Conversion on Cu(111) from Computation, ACS Catal., 5 (2015) 4020-4032.
[52] S. Sitthisa, T. Pham, T. Prasomsri, T. Sooknoi, R.G. Mallinson, D.E. Resasco, Conversion of furfural and 2-methylpentanal on Pd/SiO2 and Pd–Cu/SiO2 catalysts, J. Catal., 280 (2011) 17-27.
[53] M. Kanzaki, Y. Kawaguchi, H. Kawasaki, Fabrication of Conductive Copper Films on Flexible Polymer Substrates by Low-Temperature Sintering of Composite Cu Ink in Air, ACS Appl. Mater. Interfaces, 9 (2017) 20852-20858.
[54] M.M. Koebel, L.C. Jones, G.A. Somorjai, Preparation of size-tunable, highly monodisperse PVP-protected Pt-nanoparticles by seed-mediated growth, J. Nanopart. Res., 10 (2008) 1063-1069.
[55] S.W. Gaarenstroom, N. Winograd, Initial and final state effects in the ESCA spectra of cadmium and silver oxides, J. Chem. Phys., 67 (1977) 3500-3506.
[56] C.D. Wagner, A. Joshi, The auger parameter, its utility and advantages: a review, J. Electron. Spectrosc. Relat. Phenom., 47 (1988) 283-313.
[57] P. Scardi, M. Leoni, Whole powder pattern modelling, Acta Crystallogr. A, 58 (2002) 190-200.
[58] P. Scardi, M. Leoni, M. D'Incau, Whole Powder Pattern Modelling of cubic metal powders deformed by high energy milling, Z. Kristallogr. Cryst. Mater., 222 (2007) 129.
[59] M. Leoni, T. Confente, P. Scardi, PM2K: A flexible program implementing Whole Powder Pattern Modelling, Zeitschrift für Kristallographie Supplements, 23 (2006) 249-254.
[60] B. Ravel, M. Newville, ATHENA, ARTEMIS, HEPHAESTUS: data analysis for X-ray absorption spectroscopy using IFEFFIT, J. Synchrotron Radiat., 12 (2005) 537-541.

[61] J. Batista, A. Pintar, D. Mandrino, M. Jenko, V. Martin, XPS and TPR examinations of γ-alumina-supported Pd-Cu catalysts, Appl. Catal. A Gen., 206 (2001) 113-124.
[62] F. Cárdenas-Lizana, S. Gómez-Quero, C. Amorim, M.A. Keane, Gas phase hydrogenation of p-chloronitrobenzene over Pd–Ni/Al2O3, Appl. Catal. A Gen., 473 (2014) 41-50.
[63] S.F. Parker, H.C. Walker, S.K. Callear, E. Grünewald, T. Petzold, D. Wolf, K. Möbus, J. Adam, S.D. Wieland, M. Jiménez-Ruiz, P.W. Albers, The effect of particle size, morphology and support on the formation of palladium hydride in commercial catalysts, Chem. Sci., 10 (2019) 480-489.
[64] P.W. Albers, K. Möbus, C.D. Frost, S.F. Parker, Characterization of β-Palladium Hydride Formation in the Lindlar Catalyst and in Carbon-Supported Palladium, J. Phys. Chem. C, 115 (2011) 24485-24493.
[65] M. Mohl, D. Dobo, A. Kukovecz, Z. Konya, K. Kordas, J. Wei, R. Vajtai, P.M. Ajayan, Formation of CuPd and CuPt Bimetallic Nanotubes by Galvanic Replacement Reaction, J. Phys. Chem. C, 115 (2011) 9403-9409.
[66] M.C. Biesinger, Advanced analysis of copper X-ray photoelectron spectra, Surf. Interface Anal., 49 (2017) 1325-1334.
[67] M.C. Biesinger, B.R. Hart, R. Polack, B.A. Kobe, R.S.C. Smart, Analysis of mineral surface chemistry in flotation separation using imaging XPS, Miner. Eng., 20 (2007) 152-162.
[68] M.C. Biesinger, B.P. Payne, A.P. Grosvenor, L.W.M. Lau, A.R. Gerson, R.S.C. Smart, Resolving surface chemical states in XPS analysis of first row transition metals, oxides and hydroxides: Cr, Mn, Fe, Co and Ni, Appl. Surf. Sci., 257 (2011) 2717-2730.
[69] O.P.H. Vaughan, G. Kyriakou, N. Macleod, M. Tikhov, R.M. Lambert, Copper as a selective catalyst for the epoxidation of propene, J. Catal., 236 (2005) 401-404.
[70] A. Thøgersen, S. Diplas, J. Mayandi, T. Finstad, A. Olsen, J.F. Watts, M. Mitome, Y. Bando, An experimental study of charge distribution in crystalline and amorphous Si nanoclusters in thin silica films, J. Appl. Phys., 103 (2008) 024308.
[71] S. Hofmann, Auger- and X-Ray Photoelectron Spectroscopy in Materials Science: A User-Oriented Guide, Springer Berlin Heidelberg 2012.
[72] J. Batista, A. Pintar, J.P. Gomilšek, A. Kodre, F. Bornette, On the structural characteristics of γ-alumina-supported Pd–Cu bimetallic catalysts, Appl. Catal. A Gen., 217 (2001) 55-68.
[73] S.V. Myers, A.I. Frenkel, R.M. Crooks, X-ray Absorption Study of PdCu Bimetallic Alloy Nanoparticles Containing an Average of ∼64 Atoms, Chem. Mater., 21 (2009) 4824-4829.
[74] M. Fernández-García, J.C. Conesa, A. Clotet, J.M. Ricart, N. López, F. Illas, Study of the Heterometallic Bond Nature in PdCu(111) Surfaces, J. Phys. Chem. B, 102 (1998) 141-147.
[75] L. Guczi, Z. Schay, G. Stefler, L.F. Liotta, G. Deganello, A.M. Venezia, Pumice-Supported Cu–Pd Catalysts: Influence of Copper on the Activity and Selectivity of Palladium in the Hydrogenation of Phenylacetylene and But-1-ene, J. Catal., 182 (1999) 456-462.
[76] S. Calvin, XAFS for Everyone, Taylor & Francis, 2013.
[77] G.X. Pei, X.Y. Liu, A. Wang, A.F. Lee, M.A. Isaacs, L. Li, X. Pan, X. Yang, X. Wang, Z. Tai, K. Wilson, T. Zhang, Ag Alloyed Pd Single-Atom Catalysts for Efficient Selective Hydrogenation of Acetylene to Ethylene in Excess Ethylene, ACS Catal., 5 (2015) 3717-3725.
[78] J. Greeley, M. Mavrikakis, Alloy catalysts designed from first principles, Nat. Mater., 3 (2004) 810-815.
[79] J. Greeley, M. Mavrikakis, Near-surface alloys for hydrogen fuel cell applications, Catal. Today, 111 (2006) 52-58.
[80] J. Nilsson, P.-A. Carlsson, H. Grönbeck, M. Skoglundh, First Principles Calculations of Palladium Nanoparticle XANES Spectra, Top. Catal., 60 (2017) 283-288.
[81] S.M. Rogers, C.R.A. Catlow, C.E. Chan-Thaw, A. Chutia, N. Jian, R.E. Palmer, M. Perdjon, A. Thetford, N. Dimitratos, A. Villa, P.P. Wells, Tandem Site- and Size-Controlled Pd Nanoparticles for the Directed Hydrogenation of Furfural, ACS Catal., 7 (2017) 2266-2274.

[82] S. Sitthisa, T. Sooknoi, Y. Ma, P.B. Balbuena, D.E. Resasco, Kinetics and mechanism of hydrogenation of furfural on Cu/SiO_2 catalysts, J. Catal., 277 (2011) 1-13.
[83] V. Vorotnikov, G. Mpourmpakis, D.G. Vlachos, DFT Study of Furfural Conversion to Furan, Furfuryl Alcohol, and 2-Methylfuran on Pd(111), ACS Catal., 2 (2012) 2496-2504.
[84] S. Sitthisa, W. An, D.E. Resasco, Selective conversion of furfural to methylfuran over silica-supported NiFe bimetallic catalysts, J. Catal., 284 (2011) 90-101.
[85] S. Liu, Y. Niu, Y. Wang, J. Chen, X. Quan, X. Zhang, B. Zhang, Unravelling the role of active-site isolation in reactivity and reaction pathway control for acetylene hydrogenation, Chem. Commun., 56 (2020) 6372-6375.
[86] X. Cao, A. Mirjalili, J. Wheeler, W. Xie, B.W.L. Jang, Investigation of the preparation methodologies of Pd-Cu single atom alloy catalysts for selective hydrogenation of acetylene, Frontiers of Chemical Science and Engineering, 9 (2015) 442-449.
[87] F. Xing, J. Jeon, T. Toyao, K.-i. Shimizu, S. Furukawa, A Cu–Pd single-atom alloy catalyst for highly efficient NO reduction, Chem. Sci., 10 (2019) 8292-8298.
[88] M.M. Villaverde, T.F. Garetto, A.J. Marchi, Liquid-phase transfer hydrogenation of furfural to furfuryl alcohol on Cu–Mg–Al catalysts, Catal. Commun., 58 (2015) 6-10.
[89] F. Hu, L. Leng, M. Zhang, W. Chen, Y. Yu, J. Wang, J.H. Horton, Z. Li, Direct Synthesis of Atomically Dispersed Palladium Atoms Supported on Graphitic Carbon Nitride for Efficient Selective Hydrogenation Reactions, ACS Appl. Mater. Interfaces, 12 (2020) 54146-54154.
[90] K. Fulajtárova, T. Soták, M. Hronec, I. Vávra, E. Dobročka, M. Omastová, Aqueous phase hydrogenation of furfural to furfuryl alcohol over Pd–Cu catalysts, Appl. Catal. A Gen., 502 (2015) 78-85.
[91] M.M. Villaverde, N.M. Bertero, T.F. Garetto, A.J. Marchi, Selective liquid-phase hydrogenation of furfural to furfuryl alcohol over Cu-based catalysts, Catal. Today, 213 (2013) 87-92.
[92] S. Bhogeswararao, D. Srinivas, Catalytic conversion of furfural to industrial chemicals over supported Pt and Pd catalysts, J. Catal., 327 (2015) 65-77.
[93] H. Li, H. Luo, L. Zhuang, W. Dai, M. Qiao, Liquid phase hydrogenation of furfural to furfuryl alcohol over the Fe-promoted Ni-B amorphous alloy catalysts, J. Mol. Catal. A: Chem., 203 (2003) 267-275.
[94] R. Bardestani, R. Biriaei, S. Kaliaguine, Hydrogenation of Furfural to Furfuryl Alcohol over Ru Particles Supported on Mildly Oxidized Biochar, Catalysts, 10 (2020) 934.
[95] J. Tan, J. Cui, X. Cui, T. Deng, X. Li, Y. Zhu, Y. Li, Graphene-Modified Ru Nanocatalyst for Low-Temperature Hydrogenation of Carbonyl Groups, ACS Catal., 5 (2015) 7379-7384.
[96] P. Weerachawanasak, P. Krawmanee, W. Inkamhaeng, F.J. Cadete Santos Aires, T. Sooknoi, J. Panpranot, Development of bimetallic Ni-Cu/SiO2 catalysts for liquid phase selective hydrogenation of furfural to furfuryl alcohol, Catal. Commun., 149 (2021) 106221.
[97] J. Yu, Y. Yang, L. Chen, Z. Li, W. Liu, E. Xu, Y. Zhang, S. Hong, X. Zhang, M. Wei, NiBi intermetallic compounds catalyst toward selective hydrogenation of unsaturated aldehydes, Appl. Catal. B, 277 (2020) 119273.